Transport and Entrapment of Particles in Steel Continuous Casting

BRIAN G. THOMAS, QUAN YUAN, SANA MAHMOOD, RUI LIU,
and RAJNEESH CHAUDHARY

A particle-capture model based on local force balances has been developed, implemented into computational models of turbulent fluid flow and particle transport, and applied to simulate the entrapment of slag inclusions and bubbles during the continuous casting of steel slabs. Turbulent flow of molten steel is computed in the nozzle and mold using transient computational fluid flow models, both with and without the effects of argon gas injection. Next, the transport and capture of many particles are simulated using a Lagrangian approach. Particles touching the dendritic interface may be pushed away, dragged away by the transverse flow, or captured into the solidifying shell according to the results of a local balance of ten different forces. This criterion was validated by reproducing experimental results in two different systems. The implications of this criterion are discussed quantitatively. Finally, the fluid flow/particle transport model results and capture criterion are applied together to predict the entrapment distributions of different sized particles in a typical slab caster. More large particles are safely removed than small ones, but the entrapment rate into the solidifying shell as defects is still very high.

I. INTRODUCTION

DEFECTS in cast and rolled steel products, such as slivers and blisters, are often caused by captured inclusion clusters, slag, bubbles, and other particles.[1] During continuous casting, jets of molten steel from the submerged entry nozzle (SEN) ports carry bubbles and inclusion particles into the mold cavity from upstream processing, as shown in Figure 1.[2] In addition, droplets of liquid mold slag may become entrained into the flowing steel because of fluid flow problems, *via* several mechanisms, including meniscus level fluctuations, and excessive velocity across the slag–steel interface.[3] The particles are transported with the flow, along chaotic, circulating trajectories through the mold cavity. Particles reaching the top surface are harmlessly removed into the liquid slag layer, so long as the slag is not saturated and the surface tension forces are not excessive. Otherwise, the particles are eventually entrapped into the solidifying steel shell. Particles captured near the meniscus lead to surface defects, while particles captured deep in the caster lead to internal defects in the final steel product.

Figure 2 shows some typical inclusion particles that can be entrapped from the flowing liquid into the solidifying steel shell to form defects in continuous-cast product. Small, spherical inclusions, especially deoxidation products such as alumina, may collide together over time to form larger clusters, as in Figure 2(a).[4] Large, dendritic inclusions form when the oxygen concentration is very high, such as found during reoxidation, when the molten metal is exposed to air later during processing, as in Figure 2(b).[4] Slag entrainment often produces very large inclusions, which are spherical (Figure 2(c))[5,6] because they are still liquid when the solidifying steel entraps them. Finally, some of the argon bubbles resulting from argon gas injection into the nozzle to prevent clogging may become entrapped. These bubbles are often coated with a detrimental layer of small inclusions, as in Figure 2(d),[7] which are picked up as the bubbles move through the molten steel and its associated inclusion field.[8] During rolling, the inclusion clusters elongate to create long slivers in the final product. During subsequent annealing processes, the trapped bubbles expand to create surface blisters or pencil pipes.[9] These intermittent defects are particularly costly because they are often not detected until after many subsequent finishing steps.

Liquid steel flow and particle transport in continuous casting processes have been simulated extensively using computational models.[2,10,11] Large Eddy Simulation (LES) models can accurately calculate both the transient turbulent flow of the molten steel[12,13] and the chaotic

BRIAN G. THOMAS, C.J. Gauthier Professor, and RUI LIU, Graduate Student, are with the Department of Mechanical Science and Engineering, University of Illinois at Urbana-Champaign (UIUC), 1206 W. Green Street, Urbana, IL 61801. Contact e-mail: bgthomas@illinois.edu QUAN YUAN, Formerly Graduate Student, with the Department of Mechanical Science and Engineering, University of Illinois at Urbana-Champaign (UIUC), is now with UOP, A Honeywell Company, 25 E Algonquin Rd, Des Plaines, IL 60017. SANA MAHMOOD, Formerly Graduate Student, with the Department of Mechanical Science and Engineering, University of Illinois at Urbana-Champaign (UIUC), is now with Caterpillar Inc., 100 NE Adams Street, Peoria, IL, 61629. RAJNEESH CHAUDHARY, Formerly Graduate Student, with the Department of Mechanical Science and Engineering, University of Illinois at Urbana-Champaign (UIUC), is now with the ABB Corporate Research Center, Whitefield Road, Bangalore, 560048, Karnataka, India.
Manuscript submitted July 30, 2012.
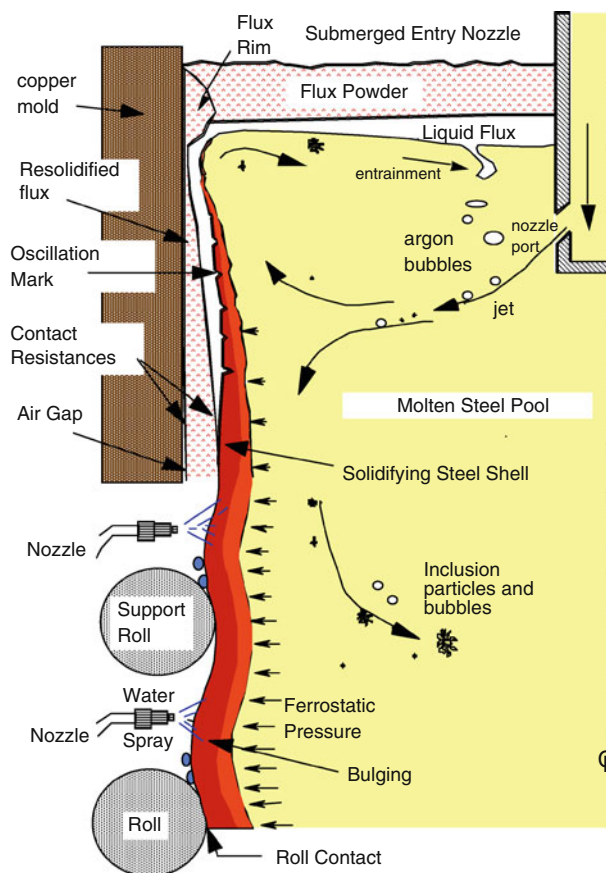Article published online August 6, 2013.

Fig. 1—Complex transport phenomena in the mold region of steel continuous casting.[2]

motion of each individual particle as it is transported through this evolving flow field.[2] Reynolds Average Navier–Stokes (RANS) and Unsteady-RANS (URANS) approaches are based on computation of the ensemble-averaged velocity field, which can make reasonably accurate predictions of the time-averaged flow pattern.[13] Particle transport through a RANS flow field can be tracked using a Lagrangian approach, introducing an extra model, such as "random walk" to generate realistic motion of every particle.[10,14–18]

There is a great incentive to optimize the mold flow pattern to minimize particle entrapment and the associated quality problems. Should the inclusion-bearing flow be directed toward the top surface to enhance particle removal, or should flow-pattern design focus instead on avoiding other problems, such as slag entrainment and level fluctuations at the top surface? To answer this and related questions requires predictive understanding of many phenomena, including a reliable criterion/model for particle entrapment into a solidification front. This is the subject of the current study.

II. PREVIOUS PARTICLE CAPTURE MODELS

Having computed the fluid velocities and particle paths, a criterion is needed to determine the fate of each particle. Particles contacting a dendritic solidification front may be captured by entrapment or engulfment,[19–23] or may be pushed along by the interface, or may drift away with the flowing liquid. Entrapment occurs easily when the particles are small enough to be surrounded by the growing dendrite arms and become captured in between them. If solidification is slow enough, large insoluble particles may be pushed by repulsive short-range Van der Waals forces along with the moving interface. Via this mechanism, the dendrite tips may push particles for large distances, leading to segregation of particles toward the centerline of metal–matrix composites, for example.[24] During this movement, liquid must flow through the thin gap between the particle and the dendrites to feed the space behind the particle. This flow creates a pressure drop which increases with front velocity, and must be sustained by local short-range repulsive forces in order to prevent the particles from slowing down and becoming "engulfed" by the dendrites. Engulfment occurs when the dendrite growth speed exceeds a critical velocity, called the pushing/engulfment transition (PET). Considerable previous study has been conducted to investigate the PET in stagnant liquid (i.e., with no cross flow).[19–21,25–33] This phenomenon depends greatly on the interfacial energy gradient, which is difficult to measure and is strongly affected by the temperature and composition gradients in the liquid which accompany solidification and segregation.[31,33,34] Finally, particles may be swept away by transverse flow across the solidification front, but this mechanism has received relatively less attention in previous studies.[35,36]

To predict the capture of inclusion particles during continuous casting of steel, previous modelers have adopted different criteria. Critical velocities for PET from previous study have not been implemented, because most are not realistic for this process, owing to their neglect of both cross-flow effects and the entrapment mechanism. Several previous models of particle transport in steel continuous casting have adopted the simple criterion that a particle becomes entrapped into the solid shell if it touches the solidification front.[17,37] However, this overpredicts the capture rate of large particles. Other models have assumed that particles reflect when they touch the solidification front, which naturally underpredicts the entrapment.[38] By including solidification into the fluid flow model, some have tracked particle transport through both the fluid and mushy regions, until the entrapped particles move with the velocity of the solid shell.[18,39] In these models, the dendritic structure that comprises the mushy zone is treated as a continuous viscous fluid, which requires an empirical treatment of the capture criterion.

Yuan and Thomas[40] have developed a fundamentally-based criterion for particle capture into a dendritic solidification front, based on a balance of local forces at the particle/dendrite contact point. This model accounts for the effects of particle properties, (size, density, and shape), Primary Dendrite Arm Spacing (PDAS), local flow field, local concentration gradients, surface tension effects, and other forces. This new methodology is summarized here, validated with measurements, and applied to predict particle entrapment in typical continuous-casters of steel slabs.
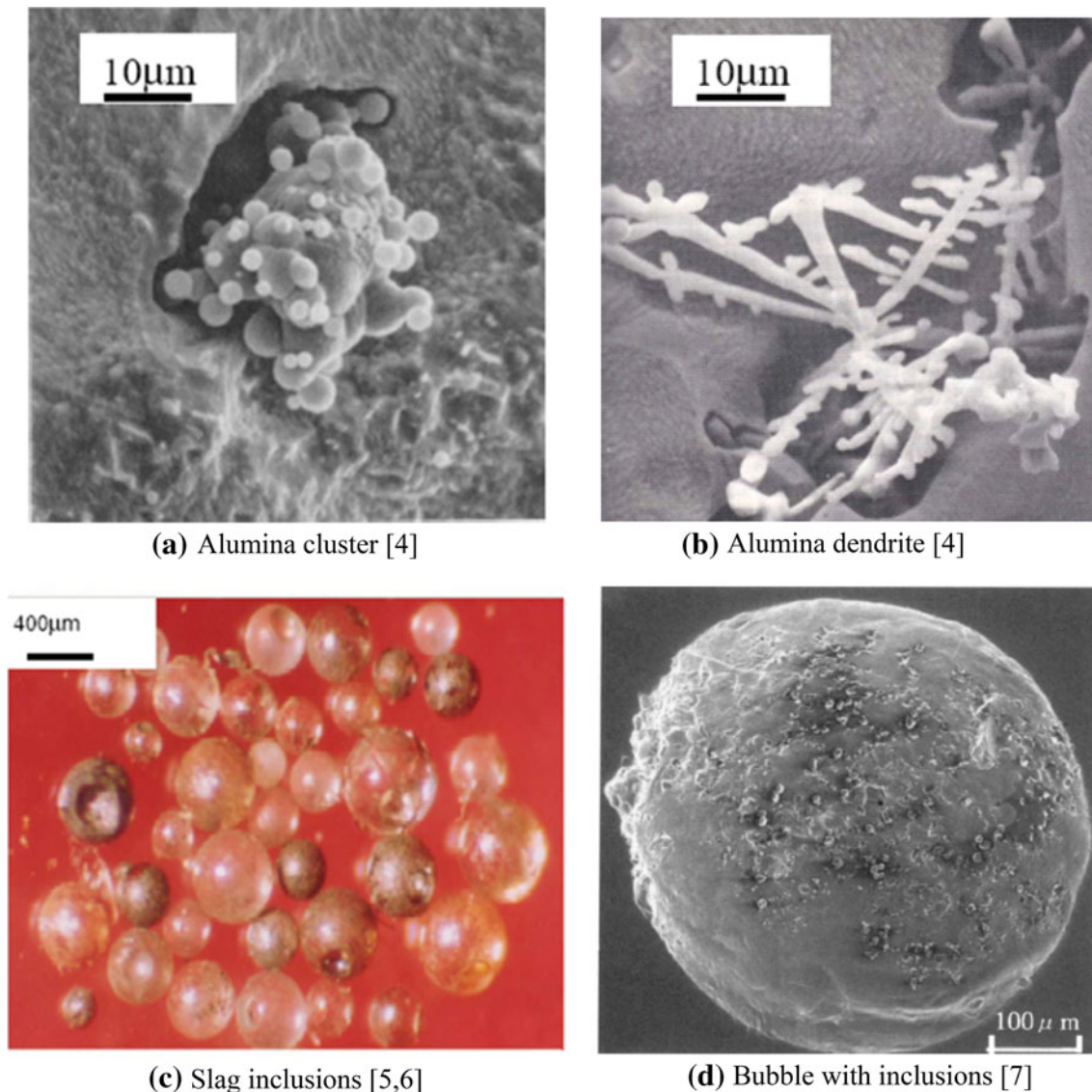
(a) Alumina cluster [4]

(b) Alumina dendrite [4]

(c) Slag inclusions [5,6]

(d) Bubble with inclusions [7]

Fig. 2—Different particle types entrapped during steel continuous casting (*a*) alumina cluster;[4] (*b*) alumina dendrite;[4] (*c*) slag inclusions;[5,6] and (*d*) bubble with inclusions.[7]

III. MODEL DESCRIPTION

Separate models are needed to predict the liquid steel flow field, particle transport, and particle capture at the solidification front.

A. *Fluid Flow Model*

Simulating the turbulent fluid flow requires solving the mass balance (continuity) and momentum balance (Navier–Stokes) equations, using LES[12] or RANS models.[14]

$$\nabla \cdot (\rho \mathbf{u}) = 0$$

$$\rho \frac{\partial \mathbf{u}}{\partial t} + \rho \mathbf{u} \cdot (\nabla \mathbf{u}) = -\nabla p + \nabla \cdot (\mu \nabla \mathbf{u}) + \mathbf{f} \qquad [1]$$

The flow domains modeled in the current study include only the liquid steel pool, as the walls represent the solidification front. This has the advantage of enabling

wall-law boundary conditions, such as the standard[41], enhanced,[14,42] or Werner–Wengle models,[43] to treat the high gradients found in the boundary layer in this region, in addition to easy identification of where/when to calculate the particle interactions with the interface. The boundary conditions at the wall enforce downward movement at the casting speed, and include mass and momentum source terms to account for mass flow across the interface.[12,44] The source term, **f**, also includes momentum contributions from the buoyancy of argon gas bubbles when there is multiphase flow,[14,45] and from turbulence. Turbulence is treated using subgrid scale models such as the wall-adapting-local eddy-viscosity (WALE) model in LES models[13,46], or the *k*-ε,[14,47] realizable *k*-ε,[13,48,49] or other turbulence model in RANS.

This approach first requires finding the shape of the liquid pool, which is accomplished in the current study using a calibrated heat-transfer model of the mold, interfacial gap, and one-dimensional solidification of

the steel shell.[50] Improved estimates of pool shape may be found using separate models of solidification and shrinkage/stress in the shell and thermal distortion of the mold.[51] Further details on the fluid-flow models used in the current study can be found elsewhere, including the transient LES model, CU-FLOW,[12,13] and the steady RANS model in FLUENT.[44,45]

B. Particle Transport Model

The motion of inclusion particles are simulated in the current study by integrating the following transport equation for the path of each particle, which considers contributions from seven different forces:

$$\frac{d\mathbf{x}_p}{dt} = \mathbf{v} \text{ where } m_p \frac{d\mathbf{v}}{dt} = \mathbf{F}_D + \mathbf{F}_B + \mathbf{F}_G + \mathbf{F}_L$$
$$+ \mathbf{F}_{added-mass} + F_{press} + F_{stress} \qquad [2]$$

The particle position, $\mathbf{x}_p$, is found from the particle velocity vector, $\mathbf{v}$, knowing the velocity field, $\mathbf{u}$, from the fluid-flow model. The terms on the right-hand side (RHS) of Eq. [2] are the drag force, buoyancy force, gravitational force, lift force, added mass force, pressure gradient force, and stress gradient force. An eighth force, Basset history force, was found to be negligible, owing to the small particles ($\leq\sim$100 μm) of interest in the current study.[40] Each of the forces in Eq. [2] is discussed next, with further details presented elsewhere.[40,44]

The drag force, $\mathbf{F}_D$, exerted on the particle by the viscous liquid tends to make it follow the fluid flow. It is calculated from Eq. [3], and depends on the particle Reynolds number, Re_p:

$$\mathbf{F}_D = \frac{1}{8}\pi d_p^2 \rho_f C_D |\mathbf{u} - \mathbf{v}|(\mathbf{u} - \mathbf{v}), \text{ where }$$
$$C_D = \frac{24}{Re_p}\left(1 + 0.15Re_p^{0.687}\right), Re_p = \frac{|\mathbf{u} - \mathbf{v}|d_p}{v} \quad [3]$$

There are two gravity-related forces: the buoyancy force, $\mathbf{F}_B$, acts upward; and the gravitational force, $\mathbf{F}_G$, acts downward (along $\mathbf{g}$). The net effect acts on the difference between the particle and fluid densities, and is calculated as follows:

$$\mathbf{F}_B + \mathbf{F}_G = \frac{(\rho_p - \rho_f)\pi d_p^3}{6}\mathbf{g} \qquad [4]$$

The lift force, $\mathbf{F}_L$, is generated by the local velocity gradients, G, across the particle. It is calculated *via* Eq. [5], with u_1 and v_1 defined as instantaneous streamwise velocities for liquid and particle, and G is the wall normal gradient of u_1.[44,52]

$$\mathbf{F}_L = -\frac{9}{4\pi}\mu d_p^2 U_s sgn(G)\left[\frac{|G|}{v}\right]^{\frac{1}{2}} J, \text{where}$$
$$G = \frac{du_1}{dy}, \varepsilon = sgn(G)\frac{\sqrt{|G|v}}{U_s}, U_s = u_1 - v_1$$
and $J(\varepsilon) = 0.6765(1 + \tanh[2.5\log_{10}\varepsilon + 0.191])$
$$(0.667 + \tanh[6(\varepsilon - 0.32)]) \qquad [5]$$

The added mass force is an unsteady force due to the acceleration of some of the fluid near a particle relative to the surrounding fluid velocity, and is calculated as

$$\mathbf{F}_{added-mass} = C_A \frac{\rho_f \pi d_p^3}{12}\left(\frac{D\mathbf{u}}{Dt} - \frac{d\mathbf{v}}{dt}\right), \text{where}$$
$$C_A = 2.1 - \frac{0.132}{0.12 + Ac^2}, Ac = \frac{|\mathbf{u} - \mathbf{v}|^2}{d_p\frac{d|\mathbf{u} - \mathbf{v}|}{dt}} \qquad [6]$$

The hydrostatic component of the pressure gradient was already included in Eq. [4] as buoyancy. The remaining nonhydrostatic component of the pressure gradient force and the stress gradient force, $\mathbf{F}_{press} + \mathbf{F}_{stress}$, are sometimes important for very low-density particles when the velocity gradients in the liquid flow field are very large, and are calculated from a rearrangement of Eq. [1] *via*

$$\mathbf{F}_{press} + \mathbf{F}_{stress} = \frac{\rho_f \pi d_p^3}{6}\frac{D\mathbf{u}}{Dt} \qquad [7]$$

These equations were coded into CU-FLOW,[12,13] and into a UDF in FLUENT for the RANS model.[44] In addition, for the RANS model, the chaotic effect of turbulence on the particle trajectories was accounted for using the random walk model:

$$\mathbf{u} = \mathbf{u} + \varsigma\sqrt{2k/3} \qquad [8]$$

With this method, the instantaneous velocity is found by adding a random number to each velocity component that is proportional to the local turbulent kinetic energy, *k,* to the mean velocity. Here, ς is a Gaussian-distributed random number, with the mean of zero and standard deviation of unity. It should be noted that for argon bubbles, the realistic motion of the bubble particles differs somewhat from the smooth paths calculated for the gas phase in multiphase flow simulations. The values of ς, and thus also the particle trajectory, remain constant for the lifetime of the largest unmodeled turbulent eddy. This eddy lifetime is itself computed using another random-number-based function of the local turbulence level.[14]

Initial simulations were performed to compare the relative importance of these seven forces in the bulk flow region.[52] The results reveal that the drag force (F_D) and the buoyancy force (F_B) are always the most significant forces. These two forces, which act in opposite directions, usually almost balance each other. The pressure and stress gradient forces, and the added mass force have approximately the same magnitude which is usually less than 15 pct of the buoyancy force. This suggests that these three forces could be neglected for engineering calculations. The lift force never exceeded from 2 to 3 pct of the buoyancy, and so is the least important force in the bulk flow region.

C. Particle Capture Model

Whenever the trajectory calculated with the particle transport model causes the particle to touch a domain

wall that represents the solidification front, a force balance is computed to determine if the particle is captured or drifts back into the flow when the local velocity field changes. In addition to the forces described in the previous section, three extra forces are exerted on particles which move close to the solidification front. They include the lubrication force, Van der Waals force, and the surface tension gradient force.

The lubrication force arising from the pressure-driven flow needed to continuously fill the thin gap between the particle, and the dendrite tip is calculated in Eq. [9],[19]

$$F_{\text{lub,n}} = 6\pi\mu V_{\text{sol}} \frac{R_{\text{p}}^2}{h_0} \left(\frac{r_{\text{tip}}}{r_{\text{tip}} + R_{\text{p}}}\right)^2 \qquad [9]$$

where μ is fluid viscosity, V_{sol} is the solidification front moving velocity, h_0 is the distance between the dendrite tip and particle, R_{p} is the particle radius, and r_{tip} is the dendrite tip radius.

The Van der Waals force for a spherical particle "touching" a convex-curved dendrite tip is given as follows[20]:

$$F_{\text{I}} = 2\pi\Delta\sigma_0 \frac{r_{\text{tip}} R_{\text{p}}}{r_{\text{tip}} + R_{\text{p}}} \frac{a_0^2}{h_0^2}, \text{ where } \Delta\sigma_0 = \sigma_{\text{sp}} - \sigma_{\text{sl}} - \sigma_{\text{pl}}$$

$$[10]$$

where σ_{sp}, σ_{sl}, and σ_{pl} represent the surface tensions for shell–particle, shell–liquid, and particle–liquid, respectively; and a_0 is the diameter of a liquid atom. This weakest of all atomic attraction forces becomes significant when the thin gap between the particle and dendrite tip, h_0, becomes small enough.

The surface tension gradient force arises because temperature and concentration gradients, due to segregation during solidification, generate different surface tensions on opposite sides of particles in the boundary layer near the solidification front. The boundaries of most particles (including entrained mold slag, argon bubbles, and dendritic clusters moving with a fluid envelope) contain flexible liquid. Thus, the surface tension on the outer (bulk-liquid) side of the particle is generally larger than that on the inside near the dendrites, and so a net force pushes the particle toward the solidification front. This force is calculated here using Eqs. [11] and [12], where the details of C^*, C_0, n, and V_{sol} are given elsewhere.[40]

$$F_{\text{Grad}} = -\frac{m\beta\pi R_{\text{p}}}{\xi^2} \left\{ \frac{\left(\xi^2 - R_{\text{p}}^2\right)}{\beta} \ln\left[\frac{(\xi + R_{\text{p}})[\alpha(\xi - R_{\text{p}}) + \beta]}{(\xi - R_{\text{p}})[\alpha(\xi + R_{\text{p}}) + \beta]}\right] \right.$$
$$\left. + \frac{2R_{\text{p}}}{\alpha} - \frac{\beta}{\alpha^2} \ln\left[\frac{\alpha(\xi + R_{\text{p}}) + \beta}{\alpha(\xi - R_{\text{p}}) + \beta}\right] \right\}$$

$$[11]$$

where $\alpha = 1 + nC_0$, $\beta = nr_{\text{tip}}(C^* - C_0)$ and $\xi = R_{\text{p}} + r_{\text{tip}} + h_0$ and C^* is calculated from

$$\frac{V_{\text{sol}} r_{\text{tip}}}{2D_{\text{s}}} = \frac{C^* - C_0}{C^*(1 - k)} \qquad [12]$$

The directions of these extra forces are shown in Figure 3(a), which shows a typical particle contacting a typical dendritic front shape, where it touches three dendrite tips. A close-up of the thin liquid film between one of the dendrite tips and a typical particle of alumina or slag is shown in Figure 3(b). For the particle to remain stationary in this moving reference frame requires fluid to continuously flow through this small gap. If the gap becomes smaller than the critical distance, h_0, then the dendrite tip can grow around the particle to entrap it.

(a) Particle touching three dendrite tips

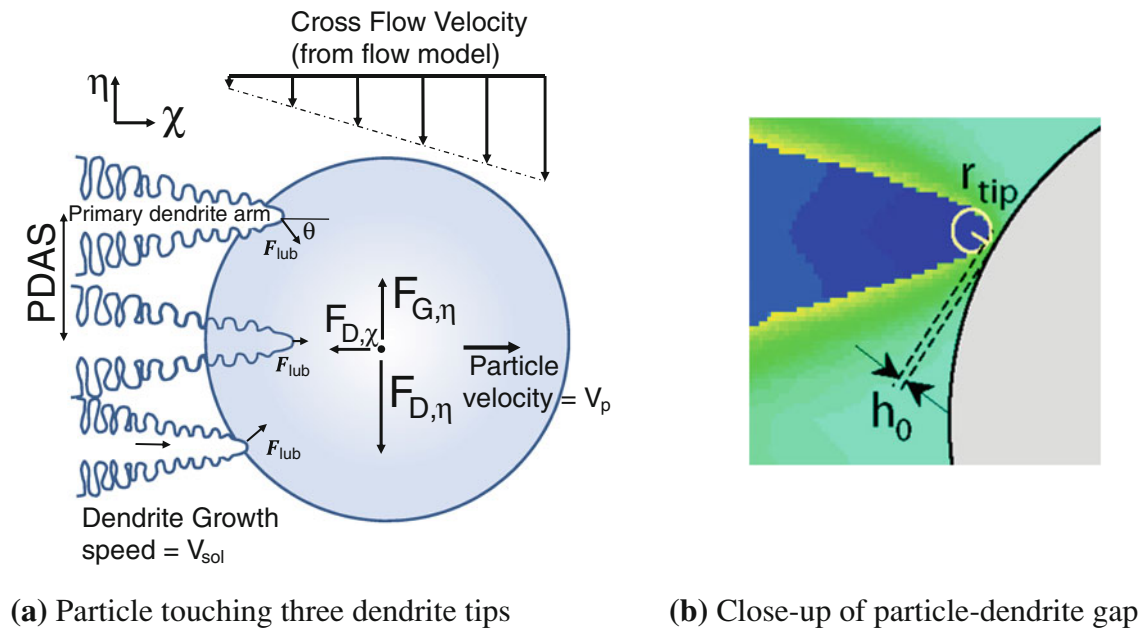**(b)** Close-up of particle-dendrite gap

Fig. 3—Force balance on a particle near a dendritic solidification front. (a) Particle touching three dendrite tips. (b) Close-up of particle-dendrite gap.

The flow chart used to model particle entrapment is given in Figure 4. Particles smaller than the local PDAS, (*i.e.*, $2R_p <$ PDAS), can travel between the dendrite arms to become captured by entrapment, whenever the trajectory touches the solidification-front boundary in the calculation. This is consistent with previous experimental studies[22] in quiescent solidification systems, which confirm that particles smaller than the PDAS are entrapped, even when the dendrite growth speed is much lower than the critical value for particle pushing.

Particles larger than the local PDAS cannot fit between the dendrite arms. If all the forces acting on a large particle are in equilibrium, then it could avoid capture by moving with the solidification front that pushes it along in the direction of solidification. This condition is checked by balancing normal force components acting on the particle in the boundary layer region, which include drag force, $F_{D,\chi}$, lift force, lubrication force, Van der Waals force, and surface tension gradient force in the normal direction to the solidification front. Usually, however, the repulsive forces in the direction of solidification are not sufficient to push the particle, and so the dendrites will grow to surround and capture it, unless the net tangential force acting across the dendrite front causes it to rotate away.

If all of the forces acting to rotate a large particle about the dendrite tips cannot balance, then the particle will avoid capture by rotating and drifting back into the flow. This condition is checked each time that the trajectory of a large particle touches a solidification-front domain wall, by computing a moment balance around the dendrite tip. This balance is dominated by the tangential drag force, $F_{D,\eta}$, and tangential buoyancy force, $F_{B,\eta}$, but is also affected slightly by the lift force, normal drag force, $F_{D,\chi}$, and the surface-tension-gradient force. The latter force is only significant in steel grades which contain large amounts of highly segregating, interfacial-active elements, such as high-sulfur steels. The pressure gradient, stress gradient, added mass, and Basset history forces are all negligible because they were found to be small (<15 pct of the buoyancy force) in the bulk region, and they are expected to be even smaller in the boundary layer. Although important for the particle pushing calculation, the lubrication and Van der Waals forces act through the pivot point at the dendrite tip, and so they do not affect this moment balance.

D. Solution Procedure

For the LES model used in the current study, the particle transport Eq. [2] was integrated using a fourth-order Runge–Kutta method.[53] Particle velocities and displacements were solved at every time step after the fluid velocity field was solved. The local fluid velocity in the drag and lift terms of Eq. [2] was interpolated from the nearest-neighbor cells using a second-order scheme.[53] Owing to the low volume fraction of impurity inclusions for the continuous casting process (~0.01 pct for a typical steel with 30 ppm oxygen), one-way coupling was employed, which neglects the modification of fluid turbulence by the particles. The removal and capture criteria were tested whenever a particle crossed a domain boundary. Particles that exit the domain bottom are assumed to eventually become entrapped.

IV. MODEL VALIDATION

A. LES Flow and Transport Model

The LES fluid flow model has been validated extensively in previous study, by demonstrating convergence with grid
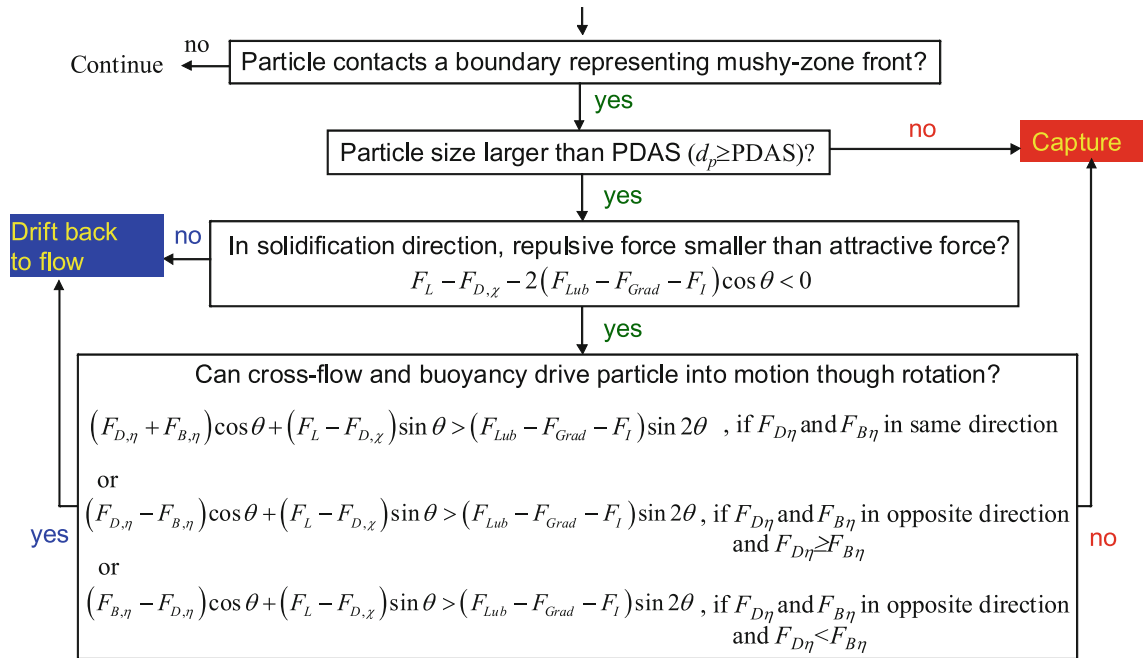
Fig. 4—Flow chart for the shell entrapment criterion.

refinement studies[54] and by successful comparison with plant measurements,[12] physical model measurements,[12,13] and with other computational models.[13,55] The particle transport model has been validated by comparing with measurements of particle residence times in water models.[2]

B. RANS Flow and Transport Model

The RANS model for fluid flow and particle transport was validated by comparing its results with the validated-LES model for simulating particle transport in a typical thin-slab caster. The LES model domain, pictured in Figure 5, includes a small portion of the bottom of the tundish and stopper rod flow control device, the entire inside of the SEN, and the top 2.4 m of the liquid pool in the strand. The RANS domain is the same, except for invoking twofold symmetry, so that only half of the mold must be modeled. The mold dimensions, properties, and casting conditions, are given in Table I, and further details are provided elsewhere.[2,12]

Sample midplane sections illustrating the predicted flow pattern from the LES model are given in Figure 6, which shows a classic double-roll recirculating flow pattern.[12] The instantaneous (left) and time-averaged flow pattern (right) are compared, based on ~70 s of simulation after the flow reached "pseudo"-steady state. The RANS model flow pattern is similar to the time-averaged LES flow pattern, which agrees with previous findings.[55] The observed velocity fluctuations are important to particle dispersal and capture. The snapshot in Figure 7 shows that the instantaneous distributions of slag inclusions predicted by the two models

agree reasonably well. In this three-port nozzle, most (88 pct) of the particles pass through the side ports, as the small central port delivers relatively little flow.
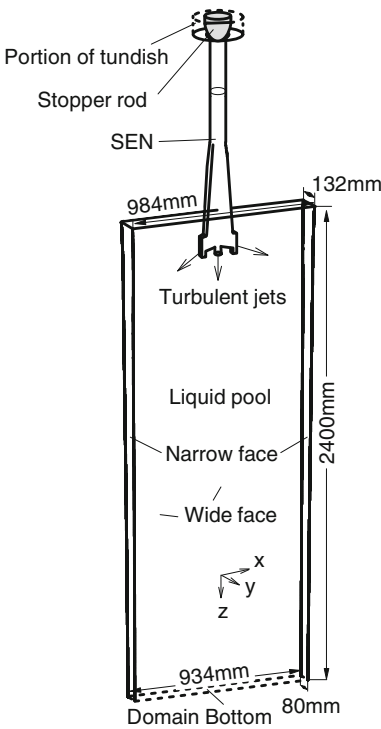

Fig. 5—Schematic of the LES domain of the thin-slab steel caster, including tundish nozzle.

Table I. Dimensions, Properties and Conditions of the Particle Simulations

| Parameter/Property	1—Thin-Slab Caster Values	2—Thick-Slab Caster Values
Steel grade	434 stainless	plain-C steel
Mold thickness (mm)	132	250
Mold width (mm)	984	1300
Mold length (mm)	1200	1300
Domain thickness (mm)		
Top	132	250
Bottom	79.5	185.1
Domain width (mm)		
Top	984	650
Bottom	934.0	619.4
Domain length (mm)	2400	3000
Nozzle port height (mm)	75	85
Port width (mm)	32	80
Bottom nozzle port diameter (mm)	32	—
SEN submergence depth (mm)	127	178
Casting speed		
(mm/s)	25.4	27.3
(m/min)	1.52	1.64
PDAS (μm)[2,44]	~50 to ~200	~50 to ~200
Steel kinematic viscosity (m^2/s)	7.98×10^{-7}	8.54×10^{-7}
Steel density (kg/m^3)	7020	7020
CFD argon gas flow rate (SLPM)	0	0, 9.2
CFD argon gas bubble size (mm)	0	0, 2.4
Particle density (kg/m^3)	2700	0.3, 2700, 5000
Particle diameter (μm)	40, 100, 250, 400	40, 100, 400, 2500
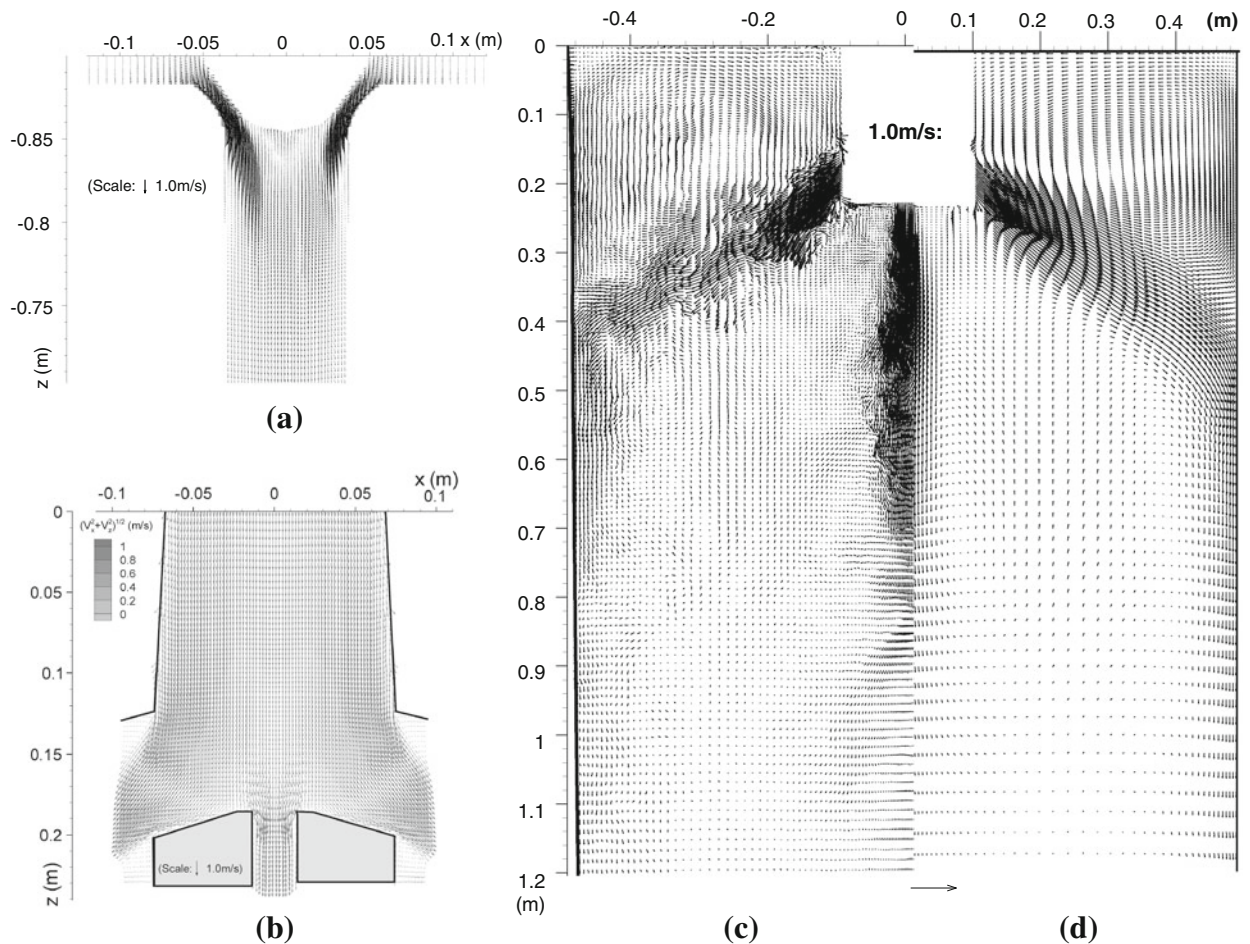
Fig. 6—Computed flow patterns (centerline between wide faces) showing time-averaged flow: (a) near stopper; (b) near nozzle ports; (c) instantaneous flow; and (d) time-averaged flow in mold region.

C. Particle Capture Model

The particle capture model has been tested by applying it in simulations of several different experimental systems where particle capture was measured. First, model predictions of the critical velocity for PET were compared with measurements of slag–droplet capture by a vertically solidifying steel dendritic interface in molten steel by Shibata[56] and zirconia particles in stagnant solidifying aluminum.[27] Simulations were then conducted to reproduce the results of the capture or flow of PMMA particles in solidifying water with a tangential (cross) flow across the interfacial ice front.[35,36] All three system produced reasonable results, as described in detail elsewhere.[52]

Finally, the particle capture model is tested by comparing the model predictions with measurements in a continuous-casting mold. The transient flow pattern, particle transport, particle entrapment, and removal rate by the top surface were simulated for the conditions (Table I thin-slab caster 1) where extensive water model and plant measurements were available.[52] The simulations assume that particles touching the top surface slag layer are removed. Some particles (~7 pct) touch the nozzle walls. The weighted averages of the final entrapment rates are given in Table II for slag inclusions for both the LES and RANS models.

Extensive plant measurements were conducted,[6] based on slime extraction of many large (500 g) samples for typical commercial conditions. The LES model predictions are consistent with the overall measurement of 78 pct of all inclusion mass entrapped, considering typical inclusion size distributions, which have more small particles, and considering the variations in the casting conditions. The RANS model appears to overpredict entrapment, however, which leads to less surface removal. This is likely due to over application of the force balance test, which should be performed only when a turbulent eddy causes the particle to touch the wall. These events are computed mechanistically with the LES model, but are estimated via the random walk behavior in RANS.

These results suggest that a significant fraction of very large particles can be removed safely into the surface slag from the mold flow. This is known from plant experience for straight-walled casters, and that is why many companies have invested in changing their top segments and molds from curved to vertical. Alternatively, the less-buoyant, easily entrapped smaller particles always experience small removal fractions. Intermediate-sized
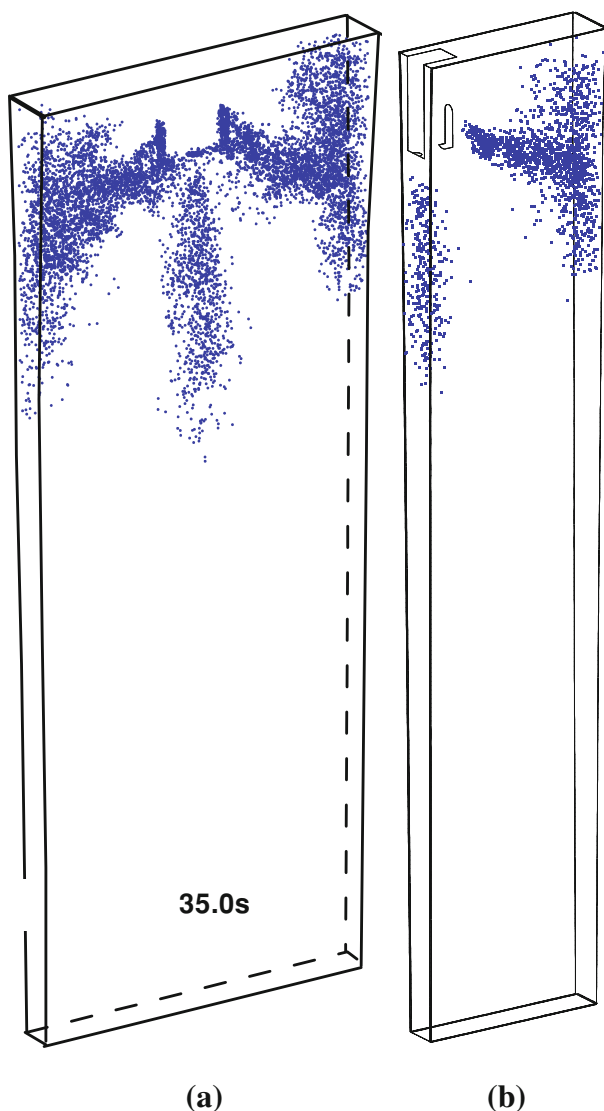
Fig. 7—Position of 40 μm slag particles after 2 s: (*a*) in full mold using LES model, and (*b*) in half mold using ($k - \varepsilon$) RANS model.

Table II. Particle Entrapment Rate: Calculation *vs* Plant Measurement

Inclusion Diameter (μm)	Entrapment (LES) (Pct)	Rate (RANS) (Pct)
40	93	97
100	88	95
250	58	89
400	30	74
Total measured[6] (tundish to slab)	78	

particles ranging from 100 to 250 μm are large enough to cause severe quality problems, yet are predicted to have high entrapment fractions, even in a vertical caster. Thus, it is important to remove inclusions from the steel during upstream steelmaking and refining stages before entering the mold.

V. CRITICAL CROSS-FLOW VELOCITIES IN CONTINUOUS STEEL CASTING

To illustrate the behavior of the particle-capture criterion, critical cross-flow velocities for the capture of different particles were computed for typical ranges of conditions found in a steel continuous caster. The flow was assumed to be vertical (upward or downward) along a horizontally growing solidification front, such as encountered near the narrow face in the mold region of a continuous caster.

The results in Figure 8 indicate that small particles (<PDAS) are always entrapped, while larger particles are only entrapped within a narrowing window of cross-flow velocity that enables a force balance to be achieved. The critical window for particle entrapment is smaller for larger particles. This is because larger particles are more easily dislodged away from the dendrite tips by a cross-flow. The critical cross-flow velocity also depends on the flow direction. Particles are more easily entrapped in downward flow, as indicated by the higher critical velocity. This is because the upward terminal velocity from buoyancy lowers the downward particle speed, while it adds to its speed in upward flow.

Figure 8(a) clearly shows that the critical downward cross-flow velocity increases with decreasing particle density. For lighter particles, more downward liquid steel momentum is needed to balance the buoyancy force, to keep the particle still at the solidification front and get captured. Figure 8(b) shows how PDAS affects the critical downward cross-flow velocity for capturing particles, using the example of argon bubbles. Increasing PDAS traps many smaller bubbles, but has less effect on larger ones. Bubbles larger than ~600 μm diameter are difficult to entrap and are relatively unaffected by PDAS. Figure 8(c) shows little effect of the solidification front velocity on critical cross-flow velocity. Figure 8(d) shows that sulfur concentration has a small but significant influence on the critical downward cross-flow velocity. Increasing sulfur content increases the entrapment of particles with size ranging from 150 to 300 μm, for the conditions studied.

Figures 8(e) and (f) show that the angle of the solidification front has a very important effect on entrapment. Relative to vertical walls (90 deg), the window for the capture of larger particles is expanded on the inner-radius of the caster, where the buoyancy force pushes particles into the solidification front, and greatly increases the likely of particle entrapment. This effect is most pronounced for very large particles, such as argon bubbles, which are known to lead to blister defects such as pencil pipe.[9] The opposite trend holds on the outer radius, where the capture window shrinks and the size of the largest particle that can ever be captured decreases to relatively small diameters (for bubbles). In addition to changes in particle trajectories, this change in the capture criterion explains why these defects can be greatly lessened with a vertical caster.

VI. PARAMETRIC STUDIES

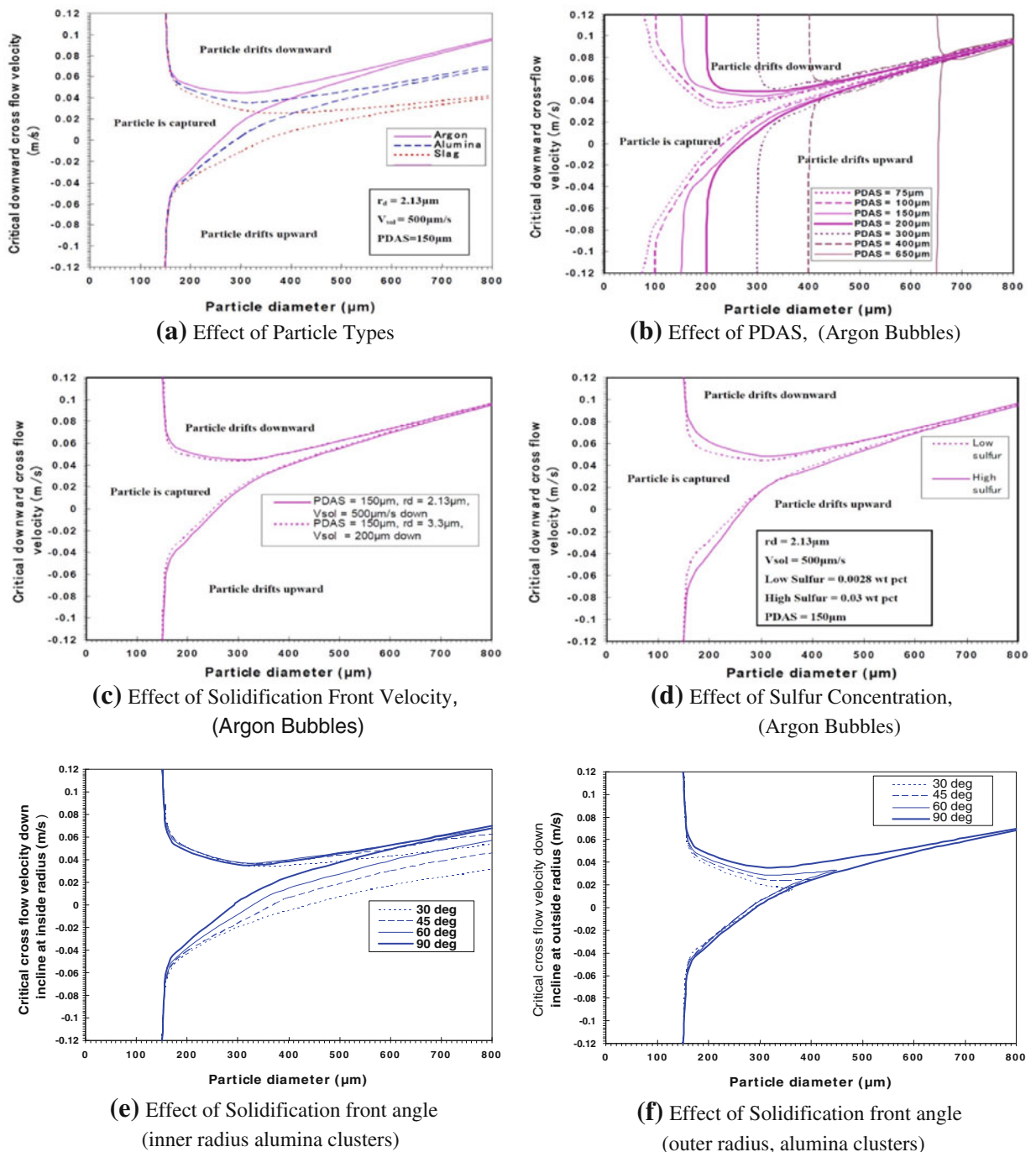The model system described and validated above for fluid flow, particle transport, and capture at the

(a) Effect of Particle Types

(b) Effect of PDAS, (Argon Bubbles)

(c) Effect of Solidification Front Velocity, (Argon Bubbles)

(d) Effect of Sulfur Concentration, (Argon Bubbles)

(e) Effect of Solidification front angle (inner radius alumina clusters)

(f) Effect of Solidification front angle (outer radius, alumina clusters)

Fig. 8—Effects on critical cross-flow velocity for particle entrapment.[44] (*a*) Effect of particle types; (*b*) effect of PDAS, (argon bubbles); (*c*) effect of solidification front velocity; (argon bubbles); (*d*) effect of sulfur concentration; (argon bubbles); (*e*) effect of solidification front angle (inner radius alumina clusters); (*f*) effect of solidification front angle (outer radius, alumina clusters).

solidification front was applied to study inclusion entrapment in typical steel continuous casters. Liquid steel flow patterns for both single-phase and argon–steel two-phase flows are computed using both the LES and RANS approaches, by tracking groups of 5000 particle trajectories each.

A. *Effect of Particle Type*

The effects of different particle types, including argon bubbles, slag droplets, and alumina inclusions were investigated by varying the size and density of the injected particles. Argon bubbles and liquid-slag droplets are accurately modeled as spherical particles with their true densities of 0.3 and 2700 kg/m^3, respectively. Alumina inclusions have complex shapes, which generate extra drag and entrap molten steel to increase their density. Dendritic alumina inclusions also may reject liquid at internal high-curvature junctions where the high surface tension may create vacuum pockets which lower density. These combined effects have been

approximated with a density of 5000 kg/m³.[57] Several sizes of each of these inclusions were simulated.

The locations of 400-μm slag particles injected through the nozzle into the thin-slab mold are shown in Figure 9 for LES model trajectory computations (instantaneous locations at 18 s of 10,000 particles) and for the RANS model (final entrapped locations of 5000 particles). The final entrapment locations are indicated in red, while blue particles are still moving. The LES distributions are asymmetric, owing to chaotic variations in the flow pattern, discussed in previous study.[2] The RANS results are similar, except for less removal at the top surface and more entrapment on the narrow face top. Figure 10 shows the evolution of particle removal from the top surface, as it increases with time, from the LES model.

The results tabulated in Table III, for the conventional thick-slab caster (RANS model), show the great effect that increasing particle size has on decreasing entrapment rate. This is because larger particles both float faster and are much easier to escape entrapment than smaller particles when they contact the shell. Also, for the same size, less-dense particles have slightly lower entrapment rates, as entrapment decreases from alumina inclusions to slag droplets to argon bubbles.
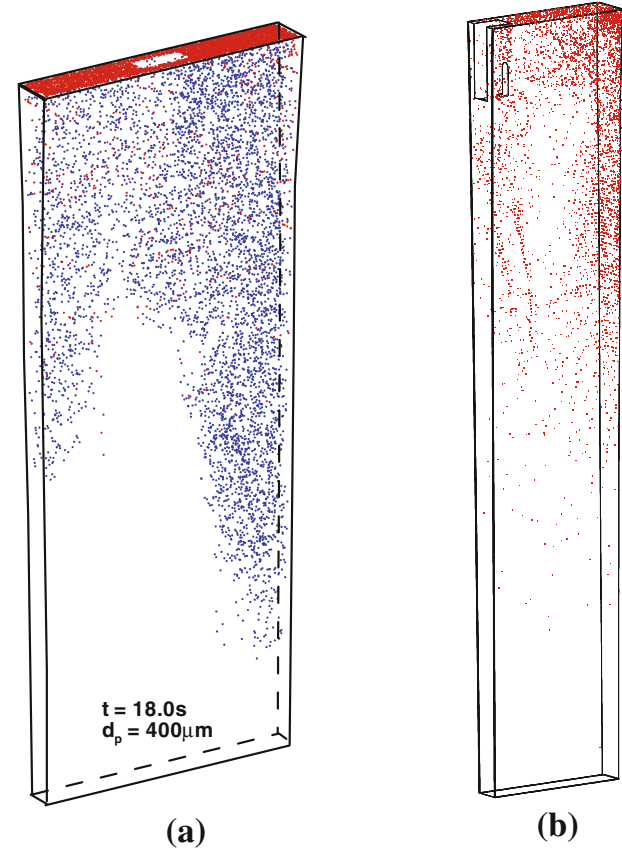
B. Effect of Multiphase Flow on Particle Entrapment

Results for four sets of 5000 slag droplets entering the thick-slab caster are shown in Figure 11 for diameters of 100 and 400 μm with and without multiphase flow. This figure confirms the dramatic increase in particle removal rate into the top surface as particle size increases, for both single- and two-phase flows. This trend agrees with previous LES and RANS results in the thin-slab caster. It is also interesting to note the greater clustering of the entrapment locations of larger particles. This is because only certain regions in the flow field achieve the narrow range of cross-flow velocities at the interface needed to capture larger particles.

Comparing surface removal rates, gas injection increases the top surface removal rate of 100-μm diameter particles by a factor of ~5, relative to single-phase flow. The removal rates of 400-μm diameter inclusions stay almost the same.

Fig. 9—Computed distribution of 400-μm slag particles injected through nozzle ports: (a) instantaneous snapshot at 18 s from LES model; and (b) final entrapment locations from RANS model.
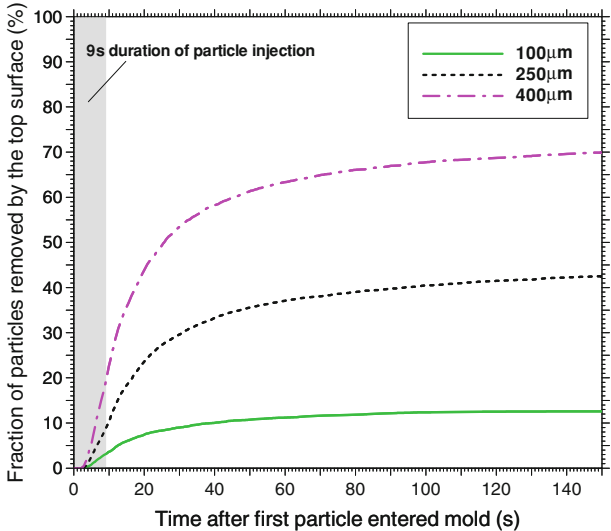

Fig. 10—Removal and entrapment histories of large slag particles (≥100 μm) which entered the mold region from nozzle ports (LES model).
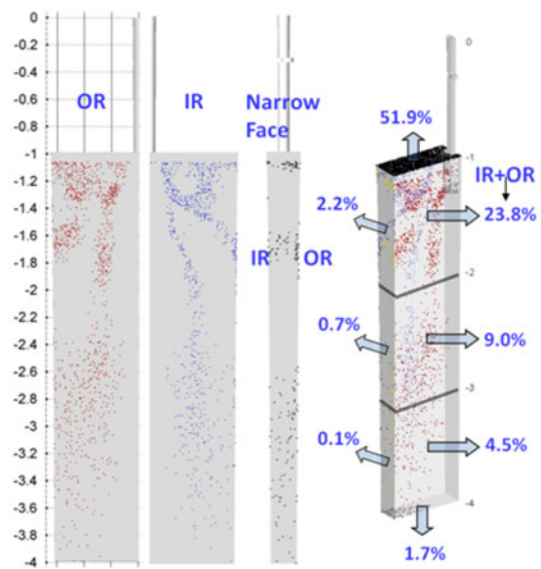
Table III. Effect of Particle Type, Size, and Flow Condition on Entrapment Rate

Inclusion Type	Diameter (μm)	Entrapment Rate Single-Phase Flow	Entrapment Rate Multiphase Flow
Slag droplet	40	98.9	90.3
	100	97.5	87.3
	400	48.1	52.1
Alumina cluster	100	98.6	88.4
Argon bubble	100	96.4	85.4
	2500	5.9	12.7
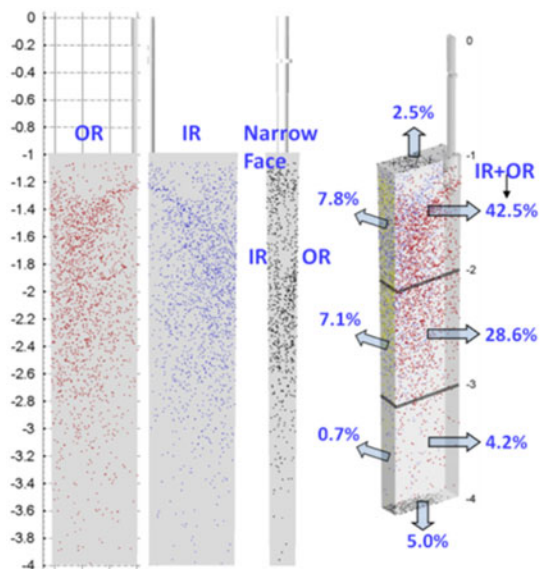
(a) Single phase flow, 100 μm slag particle

(b) Single phase, 400 μm slag particle
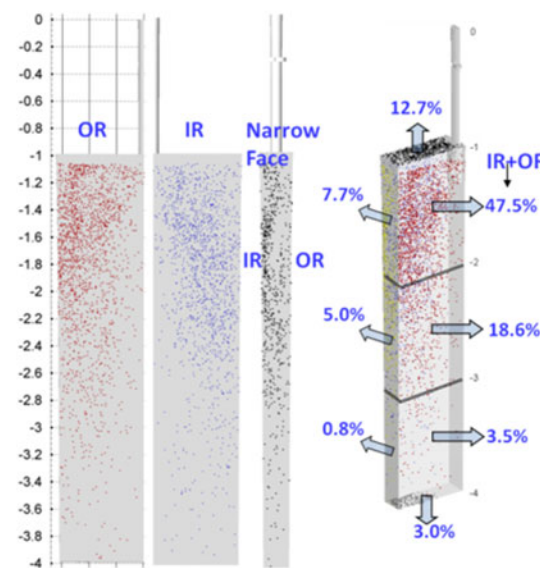
(c) Argon-steel flow, 100 μm slag particle
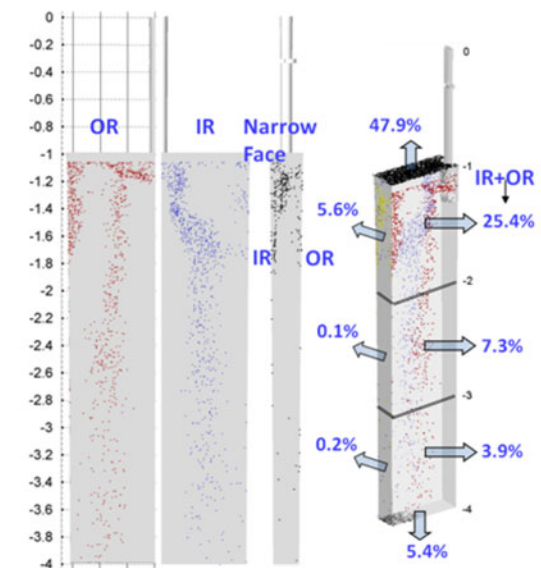
(d) Argon-steel flow, 400 μm slag particle

Fig. 11—Effects of flow pattern and particle size on particle distribution in the caster. (*a*) Single-phase flow, 100-*μ*m slag particle; (*b*) single-phase, 400-*μ*m slag particle; (*c*) argon–steel flow, 100-*μ*m slag particle; (*d*) argon–steel flow, 400-*μ*m slag particle.

VII. CONCLUSIONS

A criterion to predict particle entrapment during dendritic solidification from the results of turbulent-flow model computations is presented, validated, and applied to quantify inclusion entrapment in typical steel–slab continuous casters. The criterion considers normal and tangential force balances involving ten different forces acting on a particle in the boundary layer region near the solidification front. These forces include transverse drag, (caused by fluid flow across the dendrite interface), buoyancy (and gravity), the minor bulk hydrodynamic forces (lift, pressure gradient, stress gradient, Basset,

and added mass forces), and other forces acting at the interface (lubrication drag, Van der Waals, and surface tension gradient forces).

This capture criterion has been validated with several experimental measurements. It is then applied to predict entrapment rates for Lagrangian computations of particle transport during continuous casting of steel slabs, based on fluid velocity fields obtained from both LES and RANS simulations. The results reveal the following:

1. Particle entrapment depends mainly on the particle size and density, transverse fluid velocity from the

flow pattern, PDAS, solidification front orientation angle, and sulfur concentration gradient.

2. Increasing the number of particles improves the accuracy of removal predictions, especially for later times (*e.g.,* 10 to 100 s). At least 2500 particles are required to obtain accuracy within ±3 pct.

3. Overall particle removal rates to the top surface are small (<20 pct), and so upstream refining and prevention of reoxidation are crucial. Mold flow patterns should be optimized to avoid slag entrainment.

4. Particle removal to the top surface decreases greatly (from ~50 pct to ~10 pct) with the decreasing particle size, (from 400 to 100 *μm*) using both LES and RANS modelings of different casters.

5. Gas injection helps to increase particle removal rate at the top surface for relatively small particles (~100 *μm*), but provides not much improvement for larger particles (~400 *μm*). Adding the phenomenon of particle attachment to the gas bubbles into the model would likely increase the importance of gas injection on particle removal.

6. LES models are more accurate than RANS models which slightly overpredict particle entrapment.

NOMENCLATURE

ρ	Density (kg/m^3)
ρ_f	Liquid density (kg/m^3)
ρ_p	Particle density (kg/m^3)
u	Liquid velocity (m/s)
v	Particle velocity (m/s)
t	Time (s)
p	Pressure (Pa)
μ	Dynamic viscosity of fluid (Pa s)
v	Kinematic viscosity of fluid (m^2/s)
f	Body force density (per unit volume) (N/m^3)
$\mathbf{x}_p$	Particle position vector (m)
m_p	Mass of a particle (kg)
$\mathbf{F}_D$	Drag force (N)
$\mathbf{F}_L$	Lift force (N)
$\mathbf{F}_{\text{added-mass}}$	Added mass force (virtual mass force) (N)
$\mathbf{F}_G$	Gravitational force (N)
$\mathbf{F}_{\text{press}}$	Pressure gradient force (N)
$\mathbf{F}_{\text{stress}}$	Stress gradient force (N)
F_I	Magnitude of Van de Waals interfacial force (N)
F_{Grad}	Magnitude of surface energy gradient force (N)
F_{lub}	Magnitude of lubrication force (N)
V_{sol}	Solidification front advancing speed (m/s)
R_p	Particle radius (m)
r_{tip}	Dendrite tip radius (m)
a_0	Liquid atomic radius (m)
h_0	Distance between dendrite tip and particle (m)
$\Delta\sigma_0$	Surface energy difference (J/m^2)
σ_{sp}	Surface tension between shell and particle (J/m^2)
σ_{sl}	Surface tension between shell and liquid (J/m^2)
σ_{pl}	Surface tension between particle and liquid (J/m^2)
ξ	Distance between dendrite tip center to particle center (m)
χ	Solidification direction (m)
η	Direction across solidification (m)
g	Gravity acceleration (m/s^2)
d_p	Particle diameter (m)
C_D	Drag coefficient
Re_p	Particle Reynolds number
u_1	Streamwise liquid velocity (m/s)
v_1	Streamwise particle velocity (m/s)
U_s	Relative streamwise velocity between liquid and particle (m/s)
G	Wall normal velocity gradient of u_1 (1/s)
C_A	Correction factor on added mass force
Ac	Acceleration parameter
α	Constant for surface energy gradient force
β	Constant for surface energy gradient force (m)

REFERENCES

1. B.G. Thomas: in *Making, Shaping and Treating of Steel: Continuous Casting*, vol. 5, A. Cramb, ed., 2003, pp. 14.1–14.41.
2. Q. Yuan, B.G. Thomas, and S.P. Vanka: *Metall. Mater. Trans. B*, 2004, vol. 35B, pp. 703–14.
3. L.C. Hibbeler and B.G. Thomas: in *7th Eur. Contin. Cast. Conf.*, Dusseldorf, Germany. 2011. Vol. 1.
4. R.A. Rege, E.S. Szekeres, and W.D. Forgeng: *Met. Trans. AIME*, 1970, vol. 1, p. 2652.
5. L. Zhang and B.G. Thomas: *ISIJ Int.*, 2003, vol. 43, pp. 271–91.
6. L. Zhang, S. Yang, X. Wang, K. Cai, J. Li, X. Wan, and B.G. Thomas: *Metall. Mater. Trans. B*, 2007, vol. 28B, pp. 63–83.
7. Y. Miki and S. Takeuchi: *Iron Steel Inst. Jpn.*, 2003, vol. 43, pp. 1548–55.
8. L. Zhang, J. Aoki, and B.G. Thomas: *Metall. Mater. Trans. B*, 2006, vol. 37B, pp. 361–79.
9. W.H. Emling, T.A. Waugaman, S.L. Feldbauer, and A.W. Cramb: in *Steelmak. Conf. Proc.*, Chicago, IL. 1994. Vol. 77, pp. 371–79.
10. B.G. Thomas and L. Zhang: *ISIJ Int.*, 2001, vol. 41, pp. 1181–93.
11. B.G. Thomas: in *Making, Shaping and Treating of Steel: Continuous Casting*, vol. 5, A. Cramb, ed., AISE Steel Foundation, Pittsburgh, PA, 2003, pp. 5.1–5.24.
12. Q. Yuan, B.G. Thomas, and S.P. Vanka: *Metall. Mater. Trans. B*, 2004, vol. 35B, pp. 685–702.
13. R. Chaudhary, C. Ji, B.G. Thomas, and S.P. Vanka: *Metall. Mater. Trans. B*, 2011, vol. 42B, pp. 987–1007.
14. FLUENT6.2, User Manual, Ansys Inc., 10 Cavendish Court, Lebanon, New Hampshire, 2009.
15. B.G. Thomas, A. Dennisov and H. Bai: in *80th Steelmak. Confer. Proc.*, 1997, pp. 375–384.

16. L. Zhang, Y. Wang, and X. Zuo: *Metall. Mater. Trans. B*, 2008, vol. 39B, pp. 534–50.
17. Y. Wang and L. Zhang: *Metall. Mater. Trans. B.*, 2011, vol. 42 (6), pp. 1319–51.
18. L. Zhang, Y. Wang, E. Martinez, and K.D. Peaslee: in *CFD Modeling and Simulation in Materials*. L. Nastac, L. Zhang, B.G. Thomas, A. Sabau, N. El-Kaddah, A.C. Powell and H. Combeau, eds., TMS, Warrendale, PA, 2012, pp. 3–16.
19. D. Shangguan, S. Ahuja, and D.M. Stefanescu: *Metall. Trans. A*, 1992, vol. 23A, pp. 669–80.
20. J. Potschke and V. Rogge: *J. Cryst. Growth*, 1989, vol. 94, pp. 726–38.
21. D.M. Stefanescu and A.V. Catalina: *ISIJ Int.*, 1998, vol. 38, pp. 503–05.
22. G. Wilde and J.H. Perepezko: *Mater. Sci. Eng. A*, 2000, vol. 283, pp. 25–37.
23. Y. Wang, M. Valdez, and S. Sridhar: *Z. Metallkd.*, 2002, vol. 93, pp. 12–20.
24. J.K. Kim and P.K. Rohatgi: *Metall. Mater. Trans. B*, 1998, vol. 29A, pp. 351–75.
25. D.R. Uhlmann and B. Chalmers: *J. Appl. Phys.*, 1964, vol. 35, pp. 2986–93.
26. G.F. Bolling and J.A. Cisse: *J. Cryst. Growth*, 1971, vol. 10, pp. 55–66.
27. D.M. Stefanescu, F.R. Juretzko, B.K. Dhindaw, A. Catalina, and S. Sen: *Metall. Mater. Trans. A*, 1998, vol. 29A, pp. 1697–706.
28. D.M. Stefanescu, F.R. Juretzko, B.K. Dhindaw, A. Catalina, and S. Sen: *Metall. Mater. Trans. A*, 1998, vol. 29A, pp. 1691–96.
29. A. Catalina, D.M. Stefanescu, and S. Mukherjee: *Metall. Mater. Trans. A*, 2000, vol. 31A, pp. 2559–68.
30. G. Kaptay: *Metall. Mater. Trans. A*, 1999, vol. 30A, pp. 1887–90.
31. G. Kaptay: *Metall. Mater. Trans. A*, 2001, vol. 32A, pp. 993–1005.
32. G. Kaptay and K.K. Kelemen: *ISIJ Int.*, 2001, vol. 41, pp. 305–07.
33. G. Kaptay: *Metall. Mater. Trans. A*, 2002, vol. 33A, pp. 1869–73.
34. Z. Wang, K. Mukai, and J. Lee: *ISIJ Int.*, 1999, vol. 39, pp. 553–62.
35. Q. Han and J.D. Hunt: *J. Cryst. Growth*, 1995, vol. 152, pp. 221–27.
36. Q. Han: *The Mechanisms for Particle Pushing*, University of Oxford, Oxford, 1994.
37. B. Grimm, P. Andrzejewski, K. Muller, and K.-H. Tacke: *Steel Res.*, 1999, vol. 70, pp. 420–29.
38. Y. Wang, A. Dong, and L. Zhang: *Steel Res. Int.*, 2011, vol. 82, pp. 428–39.
39. C. Pfeiler, B.G. Thomas, M. Wu, A. Ludwig, and A. Kharicha: *Steel Res. Int.*, 2008, vol. 79, pp. 599–607.
40. Q. Yuan and B.G. Thomas: *Proc. 3rd Int. Congr. Sci. Technol. Steelmak.*, Charlotte, NC. 2005. pp. 745–62.
41. B.E. Launder and D.B. Spalding: *Comput. Method Appl. Mech. Eng.*, 1974, vol. 13, pp. 269–89.
42. B. Kader: *Int. J. Heat Mass Transf.*, 1981, vol. 24, pp. 1541–44.
43. H. Werner and H. Wengle: *8th Symp. Turbul. Shear Flows*, Munich. 1991.
44. S. Mahmood: MS Thesis, University of Illinois at Urbana-Champaign, 2006, 202 pp.
45. H. Bai and B.G. Thomas: *Metall. Mater. Trans. B*, 2001, vol. 32B, pp. 253–67.
46. F. Nicoud and F. Ducros: *Flow Turb. Comb.*, 1999, vol. 63, pp. 183–200.
47. B.E. Launder and D.B. Spalding: *Mathematical Models of Turbulence*, Academic Press, London, 1972.
48. T.H. Shih, W.W. Liou, A. Shabbir, Z. Yang, and J. Zhu: *Comput. Fluid*, 1995, vol. 24, pp. 227–38.
49. R. Chaudhary, S.P. Vanka, and B.G. Thomas: CCC Report 201017, University of Illinois at Urbana-Champaign, Aug 12, 2010.
50. Y. Meng and B.G. Thomas: *Metall. Mater. Trans. B*, 2003, vol. 34B, pp. 685–705.
51. S. Koric, L.C. Hibbeler, R. Liu, and B.G. Thomas: *Numer. Heat Transf. B*, 2010, vol. 58, pp. 371–92.
52. Q. Yuan: Ph.D. Thesis, University of Illinois at Urbana-Champaign, IL, 2004, 196 pp.
53. W.H. Press, B.P. Flannery, S.A. Teukolsky, and W.T. Vetterling: *Numerical Recipes*, Cambridge University Press, New York, NY, 1988, pp. 289–93.
54. Q. Yuan, B. Zhao, S.P. Vanka, and B.G. Thomas: *Steel Res. Int.*, 2005, vol. 76, pp. 33–43 Special Issue: Simulation of Fluid Flow in Metallurgy.
55. B.G. Thomas, Q. Yuan, S. Sivaramakrishnan, T. Shi, S.P. Vanka, and M.B. Assar: *ISIJ Int. Jpn.*, 2001, vol. 41, pp. 1262–71.
56. H. Shibata, H. Yin, S. Yoshinaga, T. Emi, and M. Suzuki: *ISIJ Int.*, 1998, vol. 38, pp. 149–56.
57. Y. Miki and B.G. Thomas: *Metall. Mater. Trans. B*, 1999, vol. 30B, pp. 639–54.